https://doi.org/10.5194/wes-2026-207
Preprint. Discussion started: 11 November 2026
© Author(s) 2026. CC BY 4.0 License.

eawe european academy of wind energy
Open Access WIND ENERGY SCIENCE DISCUSSIONS

Aeroacoustic radiation from a vertical-axis wind turbine resolved by lattice Boltzmann simulations with body-fitted overset grids

Kazuya Kusano[1] and Sota Nagatomi[2]

[1]Department of Mechanical Engineering, Yokohama National University, 79-5 Tokiwadai, Hodogaya-ku, Yokohama, 240-8501, Japan
[2]Department of Mechanical Engineering, Kyushu University, 744 Motooka, Nishi-ku, Fukuoka, 819-0395, Japan

Correspondence: Kazuya Kusano (kusano-kazuya-rp@ynu.ac.jp)

Abstract. Blade number affects both the power performance and aerodynamic noise of vertical-axis wind turbines, but their phase relationships remain insufficiently understood. This study compares one- and two-bladed straight-bladed Darrieus rotors at a tip-speed ratio of 4.5 using three-dimensional direct aeroacoustic simulations. A hybrid lattice Boltzmann method with body-fitted overset grids resolves flow, sound generation, and propagation. Compared with standard lattice Boltzmann simulations, the hybrid method predicts mean streamwise wake velocities closer to measurements, although this agreement does not validate the acoustic predictions. For both blade counts, the principal radiation peaks occur near phases of rapid change in the power coefficient rather than at maximum power. The single-blade rotor radiates most strongly during upstream passage, consistent with a contribution from rapid aerodynamic load changes at high tip-speed ratio. Adding an opposed blade increases the pressure-based radiation indicator substantially more than the mean power coefficient. Reinforcement of waves from the opposed blades may contribute, but its contribution is not separated from changes in blade loading. These findings connect blade-count effects on power performance with phase-dependent pressure radiation. The indicator includes hydrodynamic pressure fluctuations; short, unequal records and a spanwise-periodic rotor model limit generalization to turbine noise.

1 Introduction

Vertical-axis wind turbines (VAWTs) are an option for distributed wind energy generation because they can operate without yaw control and allow the generator to be installed near ground level. Their use near buildings and residential areas makes aerodynamic noise an important design consideration alongside power performance. In a straight-bladed Darrieus rotor, the relative flow velocity and angle of attack vary throughout each revolution, producing periodic changes in blade loading. The blades also encounter nonuniform flow and wakes generated during earlier passages. These unsteady aerodynamic processes can generate pressure fluctuations and sound whose strength and direction vary with rotor phase. Understanding the relationship between blade motion, loading, and acoustic radiation is therefore important for evaluating VAWT noise and developing quieter designs.

https://doi.org/10.5194/wes-2026-207
Preprint. Discussion started: 11 November 2026
© Author(s) 2026. CC BY 4.0 License.



eawe european academy of wind energy
Open Access WIND ENERGY SCIENCE DISCUSSIONS

Shubham et al. (2022) found that grid refinement affected mid- and high-frequency noise predictions more than the low-frequency contribution. In model-scale experiments, Pearson and Graham (2015) found that blade-passage harmonics generally contributed less than half the cross-spectral power above 250 Hz within the measured range. A prominent blade-passing-frequency (BPF) peak therefore does not establish periodic-noise dominance across the spectrum. Su et al. (2019) separately evaluated thickness, loading, and quadrupole contributions, identifying thickness and loading noise as the principal tonal components under their conditions. Aihara et al. (2021) predicted loading-noise dominance for a 12 kW rotor at high tip-speed ratio. Their decomposition identified the pressure-time-derivative term as a major contributor to loading noise. Botha et al. (2017) predicted inflow-turbulence-noise dominance in their investigated cases. Ottermo et al. (2017) localized higher-frequency sources near blade–strut joints, while Graham and Pearson (2022) measured noise changes caused by boundary-layer tripping, supporting a contribution from laminar instability. These findings motivate assessment of loading-related radiation with attention to geometry, operating conditions, and frequency range.

Computational fluid dynamics (CFD) has been assessed against measured VAWT loads and power curves (Bangga et al., 2020). Aeroacoustic studies have combined large-eddy simulation (Aihara et al., 2021; Ghasemian and Nejat, 2015), improved delayed detached-eddy simulation (Su et al., 2019), or lattice-Boltzmann-based very large eddy simulation (Shubham et al., 2022; Brandetti et al., 2023) with the Ffowcs Williams–Hawkings acoustic analogy. Spanwise-periodic three-dimensional calculations have also been used (Viqueira-Moreira and Ferrer, 2020). Direct aeroacoustic simulation resolves flow and sound in a common domain. Kusano et al. (2020) demonstrated this approach with a lattice Boltzmann method (LBM) for broadband airfoil noise. Resolving thin boundary layers on locally isotropic Cartesian grids also requires fine chordwise and spanwise spacing. This limitation motivated the hybrid method and computational comparisons reported by Kusano et al. (2024).

To address this cost, Kusano et al. (2024) developed a hybrid overset method coupling Cartesian-grid LBM with body-fitted finite-volume LBM (FVLBM). Cartesian LBM covers the wake and acoustic propagation region, while FVLBM permits direction-dependent refinement near moving blades. The method was validated for stationary and rotating cylinders and an isolated airfoil, and applied to a cross-flow fan. The present study uses this framework to examine how near-wall resolution and numerical treatment influence the predicted flow and pressure radiation.

Geometry effects on power and wake structure were investigated by Shubham et al. (2023), while Kuang et al. (2023) and Yushan et al. (2025) examined blade-number effects on performance and wake development, respectively. These aerodynamic studies do not establish how blade number changes acoustic radiation. A single-blade numerical reference can help examine this question by removing interactions with another blade, while retaining unsteadiness from rotation and possible encounters with its own wake. Comparison with two opposed blades must account for changes in blade loading and wake interactions as well as pressure-wave superposition; increased radiation alone cannot distinguish these contributions.

This study aims to clarify how blade number and periodic aerodynamic loading relate power performance to pressure radiation from a VAWT at high tip-speed ratio. Its distinctive contribution is a phase-resolved comparison of one- and two-bladed rotors

https://doi.org/10.5194/wes-2026-207
Preprint. Discussion started: 11 November 2026
© Author(s) 2026. CC BY 4.0 License.



eawe european academy of wind energy
Open Access WIND ENERGY SCIENCE DISCUSSIONS

that links the directly simulated pressure field to the power coefficient and its phase gradient. The hybrid LBM–FVLBM formulation follows the established method of Kusano et al. (2024); the new comparison examines how adding an opposed blade changes the strength and timing of radiation relative to power-producing loads. The single-blade reference also helps distinguish upstream and downstream contributions without assuming that changes in radiation arise solely from interference between two blades. Three-dimensional simulations are performed at a tip-speed ratio of 4.5 using a spanwise-periodic model based on the turbine geometry of Tescione et al. (2014), with blade tips, the shaft, and support struts omitted. Hybrid and standard LBM predictions of flow near the blades, mean wake velocities, and pressure spectra are compared, with wake velocities assessed against measurements (Tescione et al., 2014). Near- and far-field pressure distributions are compared between blade counts, and a phase-averaged dimensionless pressure-squared radiation indicator is related to rotor motion after accounting for propagation delay.

2 Test turbine

A straight-bladed Darrieus VAWT is considered. The two-bladed reference rotor is based on the experimental turbine of Tescione et al. (2014), with diameter $D = 1$ m, NACA0018 sections, and chord length $C = 0.06$ m. Table 1 summarizes the geometry and operating conditions. The inflow velocity is $U_\infty = 9.3$ m/s and the rotational speed is $N = 800$ rpm, corresponding to angular velocity $\omega = 2\pi N/60$. The blade-tip speed is defined as $U_{\text{tip}} = \omega D/2$, giving $U_{\text{tip}} = 41.9$ m/s for the present conditions. The tip-speed ratio is defined as $\lambda = U_{\text{tip}}/U_\infty$. The Reynolds number Re_D, based on blade-tip speed U_{tip} and rotor diameter D, is approximately 2.8×10^6. The Reynolds number Re_C, based on the same blade-tip speed and chord length C, is approximately 1.7×10^5. The experimental blade span H is 1 m, whereas the present calculation uses periodic boundaries over a computational span L_z of 0.25 times the rotor diameter. Blade tips, the shaft, and struts are omitted. The model targets unsteady flow around the blade section and the generation and propagation of pressure waves; it does not reproduce the tip flow of the finite-span experimental turbine. At 800 rpm, the blade-passing frequency (BPF), f_{BPF}, is approximately 13.3 Hz for one blade and 26.7 Hz for two blades.

Simplified rotor models have also been used to investigate blade-scale flow and performance (Ahnn and Choi, 2023). In the present study, the two-bladed configuration provides the reference for comparison with experimental wake velocities, whereas the single-blade numerical experiment provides a reference for interpreting acoustic radiation. The comparison is not intended to identify a preferred blade number for turbine design. Figure 1 shows the rotor geometry and defines the coordinate system. With the turbine center as origin, x is streamwise, y is transverse in the rotation plane, and z is along the rotor axis. The inflow is directed along positive x; rotation is counterclockwise. Azimuth θ is measured counterclockwise from positive y. Thus, $\theta = 90°$ is upstream and 270° is downstream.

https://doi.org/10.5194/wes-2026-207
Preprint. Discussion started: 11 November 2026
© Author(s) 2026. CC BY 4.0 License.



eawe european academy of wind energy
Open Access WIND ENERGY SCIENCE DISCUSSIONS

The rotor-based Reynolds number should not be equated with the chord-based Reynolds number reported for the experiment. Tescione et al. (2014) give a chord-based range of $(1.3–2.1) \times 10^5$, with a mean near 1.7×10^5. Their blades also carried 0.20 mm thick zigzag tape at 8% chord on both surfaces to promote transition. The present calculation represents the nominal NACA0018 surface rather than resolving this tape. The experimental surface treatment is relevant because subsequent analysis of the Delft rotor found appreciable changes in blade loading and wake velocity when tripped and clean airfoil characteristics were used (Rogowski et al., 2025).

Table 1. Turbine geometry and operating conditions.

Rotor diameter D	1 m
Airfoil section	NACA0018
Blade chord C	0.06 m
Inflow velocity U_∞	9.3 m/s
Rotational speed N	800 rpm
Tip-speed ratio λ	4.5
Reynolds number Re_D	2.8×10^6
Experimental blade span H	1 m (Tescione et al., 2014)
Computational span L_z	0.25 m

The one-bladed configuration is constructed by removing one blade from the two-bladed reference while retaining the airfoil section, rotor diameter, chord length, rotational speed, inflow velocity, and computational span in Table 1. It is a numerical experiment intended to observe pressure waves radiated by a single rotating blade, rather than a realistic one-bladed wind turbine. This configuration removes interactions with a second blade and its wake, simplifying the interpretation of the radiated field. The remaining blade can still encounter its own wake from earlier revolutions; the case therefore represents a single rotating blade in a periodic flow, not an isolated blade in an undisturbed inflow.

https://doi.org/10.5194/wes-2026-207
Preprint. Discussion started: 11 November 2026
© Author(s) 2026. CC BY 4.0 License.

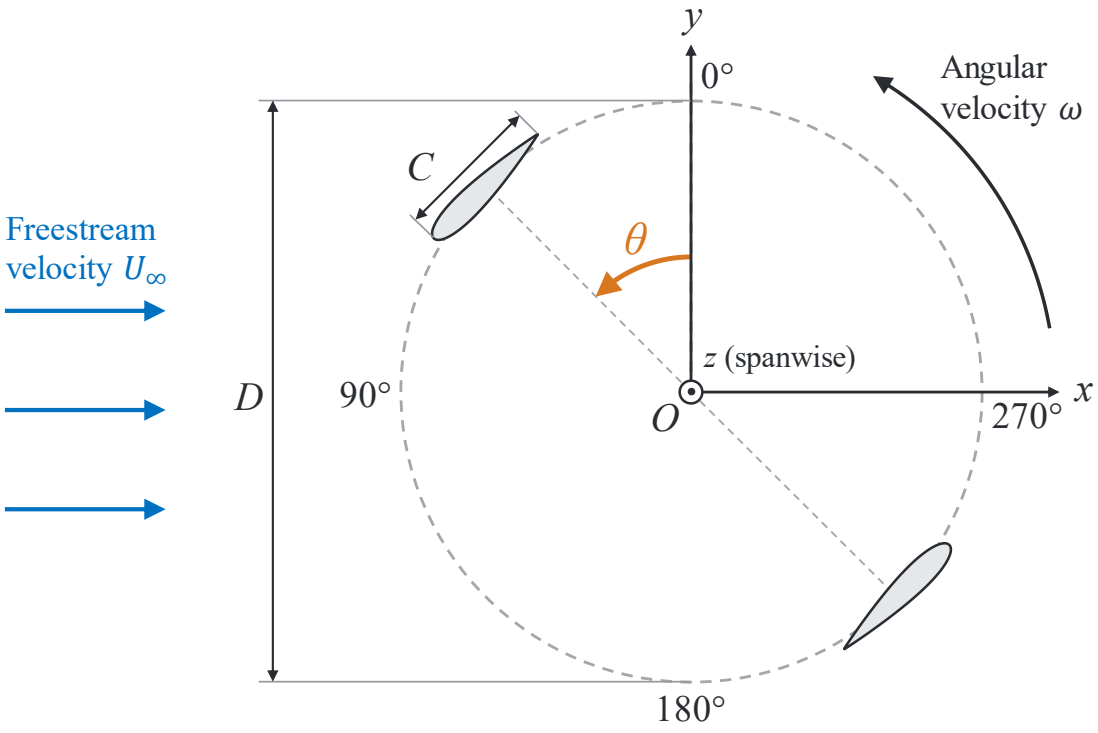


Fig. 1. Two-bladed rotor geometry, coordinates, and azimuth. Inflow is along positive x; z is spanwise. Rotation is counterclockwise, and θ is measured counterclockwise from positive y.

3 Numerical methods

LBM is a kinetic approach based on the Boltzmann equation. It evolves particle distribution functions associated with a finite set of discrete velocities, from which macroscopic density and velocity are obtained as moments. Its weakly compressible formulation represents acoustic waves through density and pressure fluctuations, allowing low-Mach-number flow and sound generation and propagation to be computed within the same framework. However, applying standard Cartesian-grid LBM to a wind turbine requires fine resolution normal to the blade surface to resolve the thin boundary layer. Because the grid spacing is isotropic, this refinement also increases resolution in the chordwise and spanwise directions, leading to a large grid-point count.

The hybrid LBM (Kusano et al., 2024) combines Cartesian-grid LBM with body-fitted FVLBM, allowing the near-wall resolution to be adjusted independently of the surrounding grid. A stationary Cartesian grid covers the flow and acoustic propagation throughout the domain, while body-fitted grids rotate with the blades and resolve the near-wall flow. The formulation follows Kusano et al. (2024). The two solvers and their coupling procedure are described below.

https://doi.org/10.5194/wes-2026-207
Preprint. Discussion started: 11 November 2026
© Author(s) 2026. CC BY 4.0 License.



eawe european academy of wind energy
Open Access WIND ENERGY SCIENCE DISCUSSIONS

3.1 LBM on Cartesian grids

On the Cartesian grid, the particle distribution function f_i is advanced according to

$$f_i(\mathbf{x} + \Delta t\mathbf{c}_i, t + \Delta t) = f_i(\mathbf{x}, t) + \Delta t\Omega_i(\mathbf{x}, t) + \Delta t F_i(\mathbf{x}, t), \tag{1}$$

where $\mathbf{x}$ denotes position, t time, Δt the time step, $\mathbf{c}_i$ the discrete particle velocity, and i the discrete velocity direction. The collision term is Ω_i, and F_i is the distribution-function source associated with external forcing. A three-dimensional 27-velocity (D3Q27) model is used. Collisions are represented by a cascaded central-moment model (Geier et al., 2006; Fei et al., 2018). A sixth-order implicit filter is applied to the distribution functions at every time step to suppress numerical oscillations at high wavenumbers (Gaitonde and Visbal, 2000).

Density ρ and momentum $\rho\mathbf{u}$ are obtained from moments of the distribution function:

$$\rho = \sum_i f_i\,, \quad \rho\mathbf{u} = \sum_i f_i\,\mathbf{c}_i \tag{2}$$

An athermal approximation neglects temperature variations in the low-Mach-number flow. Pressure p is related to density by

$$p = \rho {c_s}^2, \quad c_s = \frac{c}{\sqrt{3}}, \tag{3}$$

where c_s is the sound speed and c is the lattice velocity scale.

3.2 FVLBM on body-fitted grids

FVLBM (Xi et al., 1999) is used near each blade to permit a nonuniform body-fitted grid. Following the modified discrete Boltzmann formulation used in the hybrid method (Kusano et al., 2024), integration over a control volume with a Bhatnagar–Gross–Krook collision model gives

$$V\frac{\partial f_i}{\partial t} + \sum_\alpha S_\alpha f_i^*\mathbf{c}_i \cdot \mathbf{n}_\alpha = -\frac{V}{\tau}\left(f_i - f_i^{\mathrm{eq}}\right) + \mathcal{F}_i, \tag{4}$$

where f_i is the cell-averaged distribution function, V the cell volume, and S_α and $\mathbf{n}_\alpha$ the area and outward unit normal of cell face α, respectively. The relaxation time is τ, and f_i^{eq} is the equilibrium distribution function. The modified advective distribution f_i^* is evaluated at cell faces and is defined by $f_i^* = f_i - (a_{\mathrm{FV}}/\tau)(f_i - f_i^{\mathrm{eq}})$, with $a_{\mathrm{FV}} = 0.5$ in the solver's

https://doi.org/10.5194/wes-2026-207
Preprint. Discussion started: 11 November 2026
© Author(s) 2026. CC BY 4.0 License.



eawe european academy of wind energy
Open Access WIND ENERGY SCIENCE DISCUSSIONS

nondimensional units (Kusano et al., 2024). The stabilization parameter a_{FV} and relaxation time use the same nondimensional time convention. The forcing term $\mathcal{F}_i$ is integrated over the cell volume, whereas F_i in Eq. (1) is a source per unit volume.

The equilibrium distribution function is expressed in second-order form as

$$f_i^{\mathrm{eq}} = w_i \rho \left(1 + \frac{\mathbf{c}_i \cdot \mathbf{u}}{{c_s}^2} + \frac{(\mathbf{c}_i \cdot \mathbf{u})^2}{2{c_s}^4} - \frac{\mathbf{u} \cdot \mathbf{u}}{2{c_s}^2} \right), \tag{5}$$

where w_i is the lattice weight. For D3Q27, the weights for the rest, axial, face-diagonal, and body-diagonal velocities are 8/27, 2/27, 1/54, and 1/216, respectively.

FVLBM also uses the D3Q27 velocity model. Advective fluxes are evaluated with fourth-order central differences, a tenth-order filter is applied to the distribution functions (Gaitonde and Visbal, 2000), and time integration uses a second-order Runge–Kutta method. Calculations are performed in coordinates rotating with each blade, with centrifugal and Coriolis forces included in $\mathcal{F}_i$. Neither solver introduces an explicit subgrid-scale model. Both are treated as implicit large-eddy simulations, relying on dissipation from the numerical schemes and filters.

3.3 Overset coupling

The rotating body-fitted grids move across the stationary Cartesian grid. Coupling follows a procedure based on a direct-forcing immersed-boundary method (Kusano et al., 2024). First, Cartesian-grid LBM advances by one time step without the coupling force, updating the distribution functions and macroscopic variables. Density and velocity are then interpolated from the Cartesian grid to the outer boundaries of the body-fitted grids to supply FVLBM boundary conditions.

Local time stepping is used on the body-fitted grids: several FVLBM steps cover one Cartesian-grid time step. No-slip conditions are imposed at the blade surfaces during this integration. Finally, the FVLBM solution is fed back to the Cartesian-grid LBM through a body force, completing the coupling between the two solvers.

3.4 Computational domain, boundary conditions, and grids

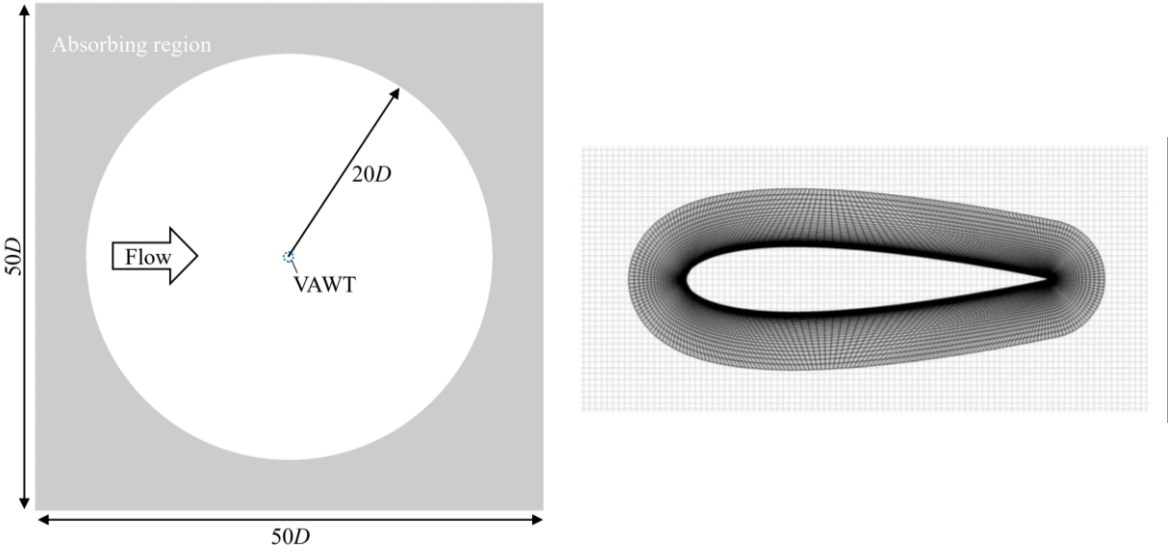
Figure 2(a) shows the computational domain. The domain spans 50 rotor diameters in each in-plane direction and 0.25 diameters axially, with periodic boundaries in z. A uniform inflow of velocity U_∞ is imposed. An absorbing region begins 20 diameters from the turbine center to reduce acoustic reflections from the outer boundaries. Blade surfaces satisfy the no-slip condition.

The Cartesian mesh comprises hierarchically arranged blocks that are uniform within each block, with local refinement around the rotor and in its wake. The minimum Cartesian grid spacing is approximately $1.6 \times 10^{-2} C$. The mesh contains approximately 1.5×10^5 blocks, each with $17 \times 17 \times 17$ grid points, giving a total of approximately 7.2×10^8 Cartesian grid points. Figure 2(b) shows the near-blade grids. At the outer boundaries of the rotating body-fitted grids, grid spacing is

https://doi.org/10.5194/wes-2026-207
Preprint. Discussion started: 11 November 2026
© Author(s) 2026. CC BY 4.0 License.

matched to the surrounding Cartesian mesh. Resolution near the blade surface can be specified independently of the Cartesian-grid resolution. The body-fitted grid has 281 points along the blade surface, 49 points in the wall-normal direction, and 257 points in the spanwise direction. Its minimum grid spacing is approximately $1.3 \times 10^{-4}C$. The Cartesian and body-fitted grids together contain approximately 730 million grid points.

For comparison, the standard LBM calculation uses only the Cartesian grid described above, with the turbine blades represented by a direct-forcing immersed-boundary method (Feng and Michaelides, 2004; Kang and Hassan, 2011). The one-bladed hybrid calculation uses the same spatial resolution as the two-bladed hybrid calculation.



(a) Computational domain (b) Blade-local mesh

Fig. 2. Computational domain and near-blade mesh. (a) Domain extending 50 rotor diameters in each in-plane direction, with acoustic absorption region beyond 20 diameters from the center. (b) Body-fitted and background Cartesian grids.

3.5 Computational implementation

Both solvers use domain decomposition with MPI processes and OpenMP threads. The two-bladed hybrid calculation uses 385 nodes of the Fugaku supercomputer, with eight MPI processes per node and six OpenMP threads per process. A flow field obtained with standard LBM provides the initial condition. The two-bladed hybrid calculation required approximately 6 s per time step, giving a total wall-clock time of approximately 917 h for 550,000 time steps.

https://doi.org/10.5194/wes-2026-207
Preprint. Discussion started: 11 November 2026
© Author(s) 2026. CC BY 4.0 License.



eawe european academy of wind energy
Open Access WIND ENERGY SCIENCE DISCUSSIONS

4 Results and discussion

4.1 Power-coefficient assessment

Figure 3 shows the time history of the power coefficient in the two-bladed hybrid-LBM simulation. The power coefficient is defined as $C_P = \omega T / \left(0.5 \rho_\infty {U_\infty}^3 D L_z\right)$, where T is the rotor torque. The standard-LBM simulation was first run from a uniform initial flow field for approximately 22 rotor revolutions (1,000,000 time steps). The resulting flow field was then used to initialize the hybrid-LBM simulation, which was run for approximately 12 additional revolutions (550,000 time steps). The initially large power-coefficient oscillations decay over the first several hybrid-LBM revolutions, and their amplitude becomes approximately stationary after seven revolutions. Two dominant oscillations occur per revolution, consistent with the two-bladed configuration. Pressure fluctuations monitored at a remote observer also indicated approximately repeatable cyclic behavior after about seven hybrid-LBM revolutions.

Table 2 compares the present power-coefficient estimates with published values for the two-bladed Delft rotor at a tip-speed ratio of 4.5. The hybrid-LBM value was calculated from the rotor torque by summing the moments of the pressure forces over the blade surfaces, with the viscous contribution neglected. Because a reliable surface-force estimate was unavailable from the present standard-LBM direct-forcing implementation, its power coefficient was estimated from the wake velocity deficit at $x/D = 0.75$. These two estimates therefore use different evaluation methods. Tescione et al. (2014) reported a predicted power coefficient of 0.40. The values selected from Rezaeiha et al. (2017) and Javaid et al. (2023) were obtained on their finest grids, containing 1,730,604 and 1,868,311 cells, respectively. Both studies used two-dimensional URANS simulations with a four-equation transition SST model. Javaid et al. considered the unmodified two-bladed NACA0018 rotor with the same diameter, chord length, free-stream velocity, and tip-speed ratio as the present case. The present torque-based coefficient uses the computational span to define the rotor swept area.

The cycle mean of the phase-averaged, torque-based power coefficient for hybrid LBM is 0.508 (Section 4.7), exceeding the published values of 0.40, 0.413, and 0.4404; it is approximately 15.4% higher than the finest-grid result of Javaid et al. Applying the same wake-based evaluation at $x/D = 0.75$ gives estimates of 0.235 for standard LBM and 0.407 for hybrid LBM. These wake-based estimates provide a comparison using a common evaluation method. Differences from the published results may also reflect the turbulence treatment, grid resolution, and modeled geometry. The present simulation uses a periodic span and omits the shaft, struts, and blade tips.

https://doi.org/10.5194/wes-2026-207
Preprint. Discussion started: 11 November 2026
© Author(s) 2026. CC BY 4.0 License.



eawe european academy of wind energy
Open Access WIND ENERGY SCIENCE DISCUSSIONS

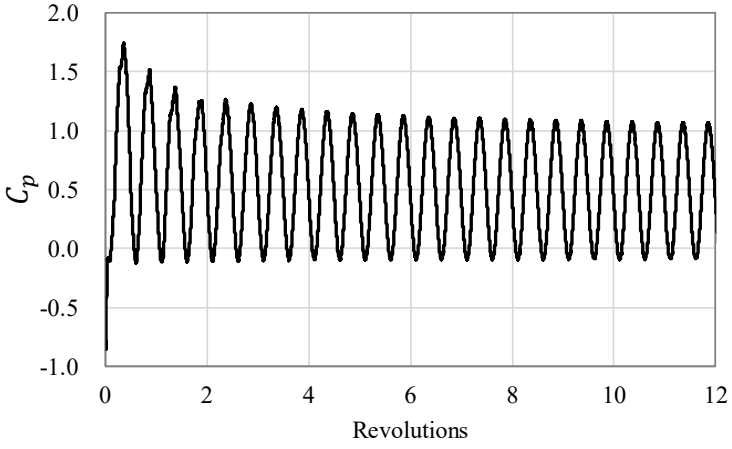


Fig. 3. Time history of the power coefficient over twelve rotor revolutions in the two-bladed hybrid-LBM simulation.

Table 2. Comparison of power-coefficient estimates for the two-bladed rotor from the present simulations and the literature.

Source / method	Power coefficient
Present standard LBM (wake-based)	0.235
Present hybrid LBM (torque-based)	0.508
Tescione et al. (2014)	0.40
Rezaeiha et al. (2017)	0.413
Javaid et al. (2023)	0.4404

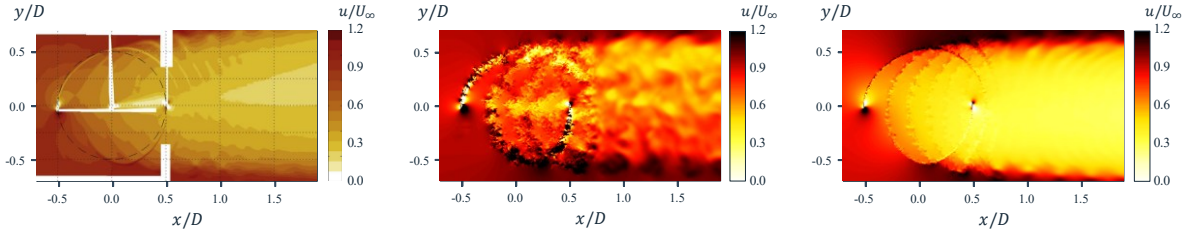
205

4.2 Comparison of wake velocities with measurements

Figures 4 and 5 compare the streamwise velocity u and transverse velocity v fields near $\theta = 90°$. The experimental fields are phase averaged, whereas the numerical fields are instantaneous. Standard LBM predicts less downstream deceleration than both the experiment and hybrid LBM (Fig. 4), consistent with its lower wake-based power-coefficient estimate in Section 4.1.
210 It also produces more pronounced small-scale velocity variations within and downstream of the rotor than hybrid LBM. However, phase averaging suppresses nonperiodic fluctuations in the experimental fields, so differences in smoothness do not directly measure numerical accuracy. These instantaneous comparisons identify qualitative differences in the velocity distributions; the mean profiles below provide a more direct comparison with the measurements. The experimental and

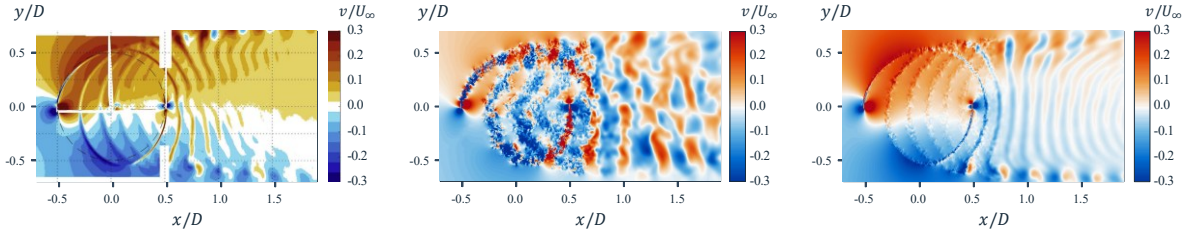
https://doi.org/10.5194/wes-2026-207
Preprint. Discussion started: 11 November 2026
© Author(s) 2026. CC BY 4.0 License.

numerical color maps differ despite using the same numerical ranges, so comparisons should be based on velocity values and spatial patterns rather than color alone.



(a) Experiment (b) Standard LBM (c) Hybrid LBM

Fig. 4. Streamwise velocity u/U_∞ at $\theta = 90°$. (a) Phase-averaged experiment; (b) instantaneous standard LBM; (c) instantaneous hybrid LBM. Coordinates are normalized by D. The numerical ranges are common, but experimental and numerical color maps differ. Experimental data: Tescione et al. (2014).



(a) Experiment (b) Standard LBM (c) Hybrid LBM

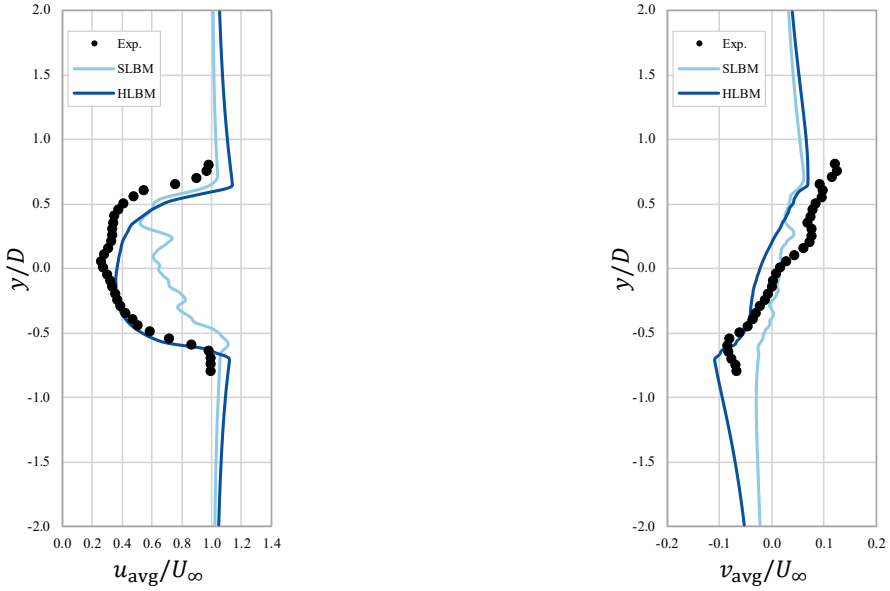
Fig. 5. Transverse velocity v/U_∞ at $\theta = 90°$. (a) Phase-averaged experiment; (b) instantaneous standard LBM; (c) instantaneous hybrid LBM. Coordinates are normalized by D. The numerical ranges are common, but experimental and numerical color maps differ. Experimental data: Tescione et al. (2014).

Figure 6 compares the mean streamwise and transverse velocity profiles at $x/D = 0.75$. For the streamwise component (Fig. 6(a)), standard LBM overpredicts the velocity near the wake center and consequently underpredicts the velocity deficit. Hybrid LBM predicts a larger deficit and agrees more closely with the measurements, particularly from the wake center toward negative y/D. Discrepancies remain near the positive-y/D wake edge, where the measured increase in streamwise velocity toward the outer flow is not fully reproduced. Outside the wake, the numerical profiles show velocities slightly above the inflow velocity, whereas this acceleration is less evident in the measurements. This difference may arise from the way the flow passes around the rotor. Because the spanwise-periodic model excludes flow around the blade tips, the flow bypasses the rotor in the transverse (y) direction, potentially enhancing blockage-induced acceleration outside the wake. In the finite-span experiment, flow can also pass around the blade tips in the spanwise direction, which may reduce the acceleration of the flow outside the wake.

For the transverse component (Fig. 6(b)), both methods reproduce the measured change from negative velocity on the negative-y/D side to positive velocity on the positive-y/D side. Hybrid LBM agrees more closely with the measurements over part of the negative-velocity region, but underpredicts the positive velocities and does not reproduce the measured zero-crossing

https://doi.org/10.5194/wes-2026-207
Preprint. Discussion started: 11 November 2026
© Author(s) 2026. CC BY 4.0 License.

location. The spanwise-periodic model omits blade tips, the shaft, and struts and cannot reproduce the full three-dimensional wake evolution measured by Tescione et al. (2014). The experimental blades were tripped, whereas the simulations use the nominal airfoil geometry. These geometric and surface-treatment differences limit attribution of the discrepancies in Fig. 6 to the near-wall numerical treatment alone.



(a) Streamwise velocity (b) Transverse velocity

Fig. 6. Mean wake velocity profiles at $x/D = 0.75$. (a) Streamwise velocity; (b) transverse velocity. Black symbols: experiment, Tescione et al. (2014); light blue: standard LBM; dark blue: hybrid LBM. Velocity and transverse position are normalized by U_∞ and D, respectively.

4.3 Relative flow near the blade

Figure 7 compares the instantaneous relative velocity $\mathbf{w}$ in a reference frame fixed to and rotating with the blade at nominal azimuths of 0°, 90°, 180°, and 270°. The coordinates s and n denote the chordwise and chord-normal directions, respectively, and the arrows indicate the velocity direction relative to the blade. In standard LBM, a low-speed region extends along the upper surface at $\theta = 0°$. At $\theta = 90°$, a larger low-speed region extends along the lower surface and downstream of the trailing edge, while at $\theta = 270°$ a nonuniform low-speed region extends from the upper surface into the wake. These extended low-speed regions suggest separated flow, although velocity magnitude alone does not establish the extent of separation.

In hybrid LBM, the low-speed regions at these phases remain closer to the blade surface and trailing edge, with less extensive disturbances in the surrounding relative flow. These differences accompany the closer agreement with the measured mean streamwise wake profile in Fig. 6(a) and the higher wake-based power-coefficient estimate in Section 4.1. Together, the results

https://doi.org/10.5194/wes-2026-207
Preprint. Discussion started: 11 November 2026
© Author(s) 2026. CC BY 4.0 License.

suggest a link between the numerical representation of the near-blade flow and the predicted rotor wake and aerodynamic performance. The finer wall-normal resolution provided by the body-fitted grid, together with the different wall treatment, may contribute to the improved wake prediction. These observations are limited to the tip-speed ratio of 4.5 examined here.

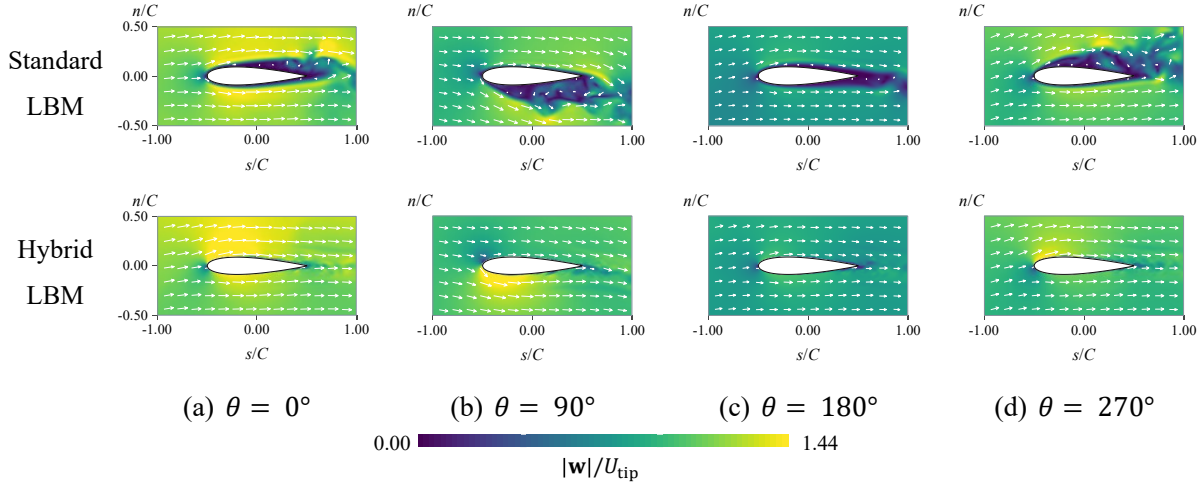


Fig. 7. Instantaneous relative velocity viewed in a reference frame fixed to and rotating with the blade at a tip-speed ratio of 4.5. Columns (a)–(d): $\theta = 0°$, 90°, 180°, and 270°. Top: standard LBM; bottom: hybrid LBM. Colors show $|\mathbf{w}|/U_{\mathrm{tip}}$; arrows indicate velocity relative to the blade. s and n are the chordwise and chord-normal coordinates, respectively, both normalized by chord C.

4.4 Pressure spectra and numerical-method effects

Figure 8 compares the power spectral density (PSD) of pressure fluctuations predicted by standard and hybrid LBM for the two-bladed rotor. The observer is located ten rotor diameters from the rotor center in the direction perpendicular to the inflow. Each pressure time series was divided into three segments with 50% overlap. The spectra of the individual segments were then averaged to estimate the PSD with a frequency resolution of 3.7 Hz.

Both methods predict a dominant peak near 27 Hz, consistent with the blade-passing frequency (BPF) of 26.7 Hz, and a secondary peak near 53 Hz, consistent with its second harmonic. Hybrid LBM predicts higher spectral levels near and below the BPF, whereas standard LBM produces more pronounced, closely spaced peaks over part of the 100–500 Hz range. These higher-frequency differences may be related to the more extensive low-speed regions observed near the blade in standard LBM (Section 4.3), which suggest separated flow. The comparison raises the possibility that the coarser near-wall resolution and wall treatment in standard LBM introduce excess high-frequency spectral content.

https://doi.org/10.5194/wes-2026-207
Preprint. Discussion started: 11 November 2026
© Author(s) 2026. CC BY 4.0 License.



eawe european academy of wind energy
Open Access WIND ENERGY SCIENCE DISCUSSIONS

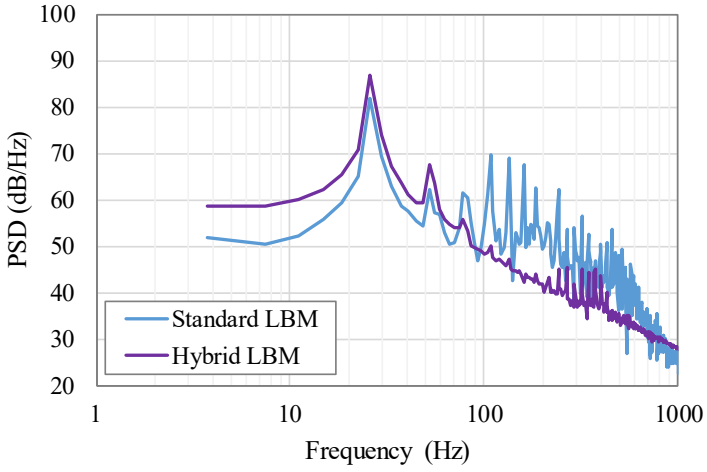


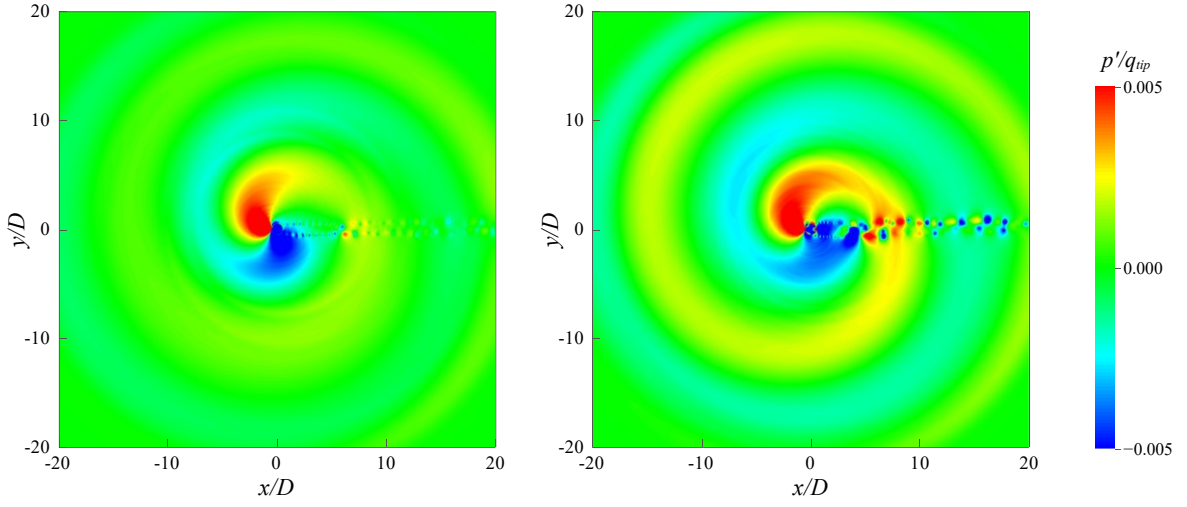
Fig. 8. Power spectral density of pressure fluctuations for the two-bladed rotor at a tip-speed ratio of 4.5. The observer is located ten rotor diameters from the rotor center in the direction perpendicular to the inflow. Blue: standard LBM; purple: hybrid LBM. The reference pressure for the decibel scale is 2.0×10^{-5} Pa.

4.5 Far-field pressure radiation

To examine how blade number affects pressure radiation, the two-bladed rotor is compared with the single-blade numerical experiment. Figure 9 shows the instantaneous far-field pressure fluctuations from the hybrid simulations at a blade azimuth of approximately 90°. Pressure fluctuations are normalized by the dynamic pressure based on the blade-tip speed, $q_{\mathrm{tip}} = 0.5\rho_{\infty}{U_{\mathrm{tip}}}^{2}$.

Spiral-like wavefronts extend outward from both rotors. For two blades, alternating positive and negative pressure bands are more distinct and remain visible over a larger radial extent than for one blade under the common color scale. No pronounced directional concentration of these bands is apparent in the two-bladed snapshot. In both cases, localized pressure fluctuations also form a sequence along the downstream wake, superposed on the outward-propagating field. The displayed pressure therefore contains wake-related contributions as well as radiating waves; the downstream-sector exclusion used in Section 4.7 reduces the influence of these contributions on the radiation indicator.

https://doi.org/10.5194/wes-2026-207
Preprint. Discussion started: 11 November 2026
© Author(s) 2026. CC BY 4.0 License.



(a) One blade (b) Two blades

Fig. 9. Instantaneous far-field pressure fluctuations from hybrid LBM. (a) One blade; (b) two blades. Phase: $\theta = 90°$; tip-speed ratio: 4.5. Results are shown in the midspan plane $z = 0$.

4.6 Near-field pressure fluctuations

Figure 10 compares the instantaneous near-field pressure fluctuations at blade azimuths of approximately 0°, 45°, 90°, and 135°, with the one-bladed results in the left column and the two-bladed results in the right column. The fluctuations are obtained by subtracting the time-averaged pressure from the instantaneous pressure. A sharp contrast between the rotor interior and exterior, also present in the time-averaged field, remains visible in the fluctuation maps. This spatial feature should be distinguished from the pressure disturbances that extend outward from the rotor.

In the one-bladed case, the pressure pattern near the blade rotates with it. With two blades, positive and negative fluctuations develop around the opposing blades, and their distribution within and outside the rotor changes with phase. At several displayed phases, the pressure fluctuations on the inner and outer sides differ in sign between the opposing blades. The additional blade thus changes the phase-dependent pressure distribution both inside and outside the rotor.

https://doi.org/10.5194/wes-2026-207
Preprint. Discussion started: 11 November 2026
© Author(s) 2026. CC BY 4.0 License.

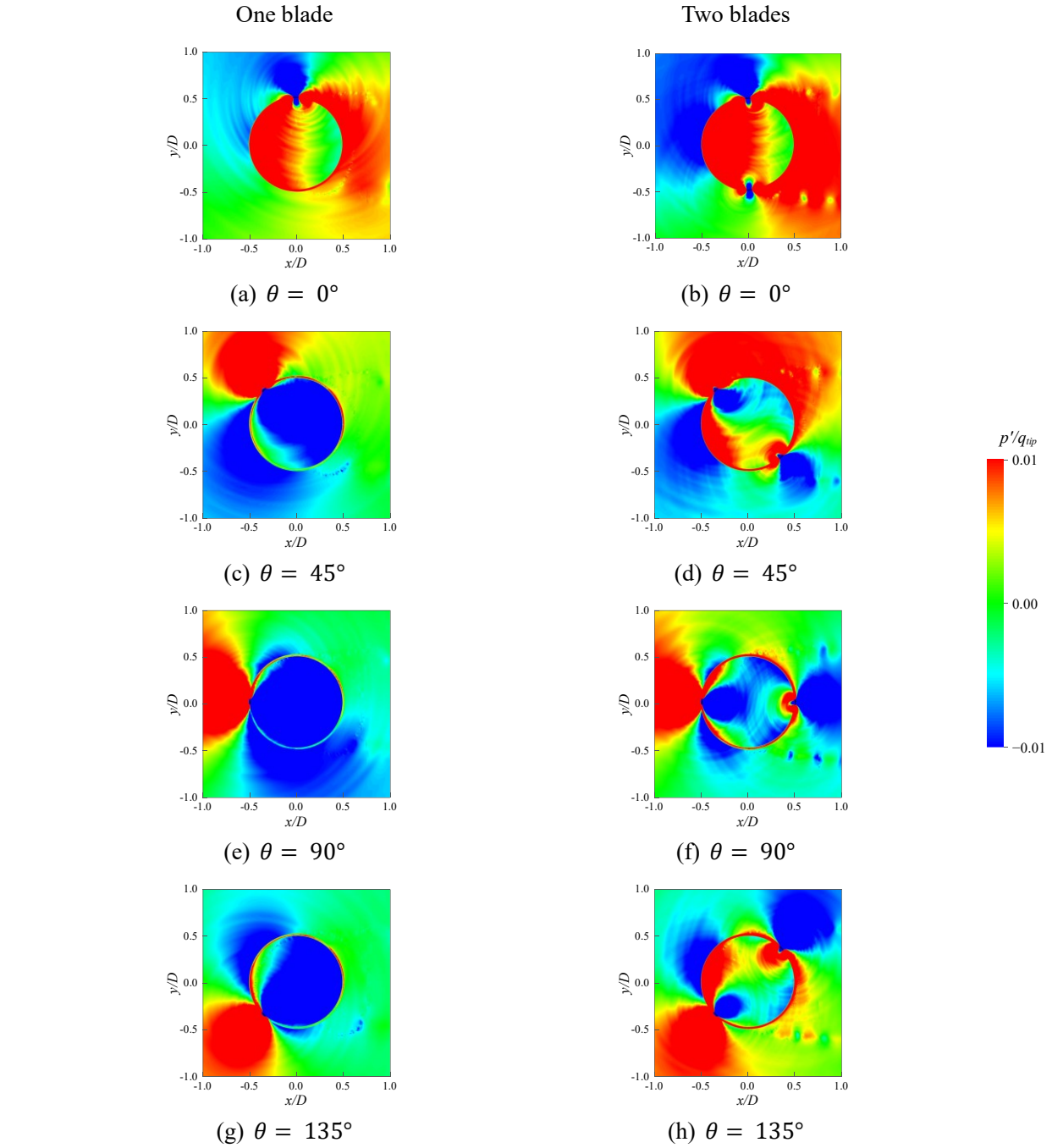


Fig. 10. Instantaneous near-field pressure fluctuations from hybrid LBM. Left column: one blade; right column: two blades. Rows from top to bottom: approximately 0°, 45°, 90°, and 135°. Tip-speed ratio: 4.5. Results are shown in the midspan plane $z = 0$.

Figure 11 extends this comparison by showing pressure fluctuations around the circle $r/D = 1$. The horizontal coordinate, blade azimuth θ, describes the rotor phase at the observation time; the vertical coordinate, observer angle ψ, identifies a fixed

https://doi.org/10.5194/wes-2026-207
Preprint. Discussion started: 11 November 2026
© Author(s) 2026. CC BY 4.0 License.



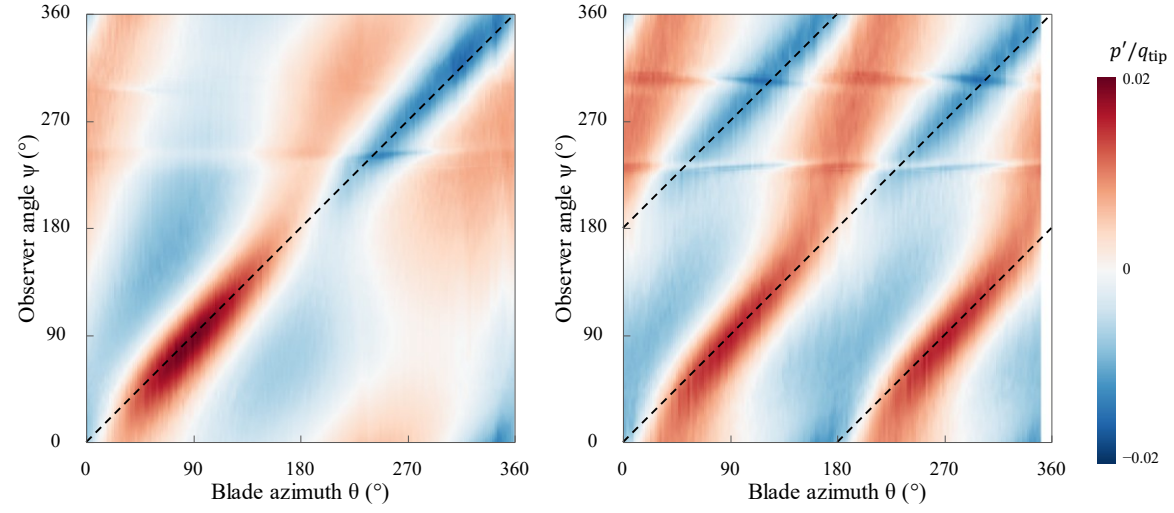
eawe european academy of wind energy
Open Access WIND ENERGY SCIENCE DISCUSSIONS

sampling position on the circle. Both are measured counterclockwise from the positive transverse axis. Reading the map vertically gives the circumferential pressure distribution at one instant, whereas reading it horizontally gives the pressure variation at a fixed observer as the rotor turns. The dashed lines identify observer directions aligned with the instantaneous blade positions; the two blades are separated by 180°. The sampling circle lies outside the blade trajectory, so these lines indicate angular alignment rather than passage through a sampling point.

Diagonal bands of positive and negative pressure fluctuations follow the progression of blade azimuth. Along the blade-direction lines, the fluctuations are predominantly positive when the corresponding blade lies in the upstream half of the rotor and negative when it lies in the downstream half, with sign changes near the transitions between the two halves. This phase dependence is consistent with changes in blade loading during rotation. Over the sampled phases, the one-bladed case has larger pressure extrema along these lines. The two-bladed map shows an approximately repeating pattern at 180° intervals. Larger local extrema in the one-bladed case do not, however, establish stronger acoustic radiation. In the one-bladed map, weaker fluctuations of the same sign also occur near the direction opposite the blade. Their presence suggests that disturbances associated with one blade may contribute to the pressure field near the opposing blade in the two-bladed rotor. Superposition could therefore contribute to the more distinct external pressure bands in Fig. 9. This comparison does not isolate interference, because adding a blade also changes the flow and blade loading.

Nearly horizontal bands occur downstream at observer angles of approximately 230–245° and 295–310°, with their positions differing between the two cases. These bands remain near fixed observer directions as the rotor turns, in contrast to the diagonal bands that follow blade motion. Their downstream locations and temporal variation are consistent with wake-related pressure fluctuations. Because near-field pressure contains both hydrodynamic and acoustic contributions, the local fluctuation amplitude cannot be interpreted directly as radiated sound intensity.

https://doi.org/10.5194/wes-2026-207
Preprint. Discussion started: 11 November 2026
© Author(s) 2026. CC BY 4.0 License.



(a) One blade (b) Two blades

Fig. 11. Pressure fluctuations on the circle $r/D = 1$ at $z = 0$ for a tip-speed ratio of 4.5. (a) One blade; (b) two blades. Horizontal axis: blade azimuth θ at the observation time. Vertical axis: observer angle ψ on the sampling circle. Dashed lines identify observer directions aligned with the instantaneous blade positions; the two blades are separated by 180°.

4.7 Radiation indicator and phase-dependent power

A dimensionless radiation indicator is used to examine how pressure radiation varies with blade phase. The indicator is based on the phase average of squared pressure fluctuations around a common observer circle. To compare pressure with rotor motion, the propagation delay is approximated using the distance R from the rotor center and the sound speed c_s. The observation time t then gives the estimated source time t_s and source phase θ_s:

$$t_s = t - \frac{R}{c_s}, \quad \theta_s(t) = \theta(t_s) \tag{6}$$

The observer circle has radius $R/D = 16$. To reduce contamination by downstream hydrodynamic pressure fluctuations, directions within 20° of the downstream direction ($\psi = 270°$) are excluded. The integral covers the remaining 320° of the circle, from 0° to 250° and from 290° to 360°, with angular integration evaluated in radians. The dimensionless radiation indicator is defined as:

$$C_{\mathrm{rad}}(\theta) = \frac{R}{D}\int \left\langle \left(\frac{p'(R,\psi,t)}{q_{\mathrm{tip}}}\right)^2 \right\rangle_{\theta} d\psi \tag{7}$$

https://doi.org/10.5194/wes-2026-207
Preprint. Discussion started: 11 November 2026
© Author(s) 2026. CC BY 4.0 License.



eawe european academy of wind energy
Open Access WIND ENERGY SCIENCE DISCUSSIONS

where p' is the pressure fluctuation relative to the time-averaged pressure, and $\langle\cdot\rangle_\theta$ denotes an average at the same corrected blade phase. The pressure fluctuation is normalized by q_{tip} and squared before phase averaging. A larger C_{rad} indicates a larger phase average of normalized pressure squared over the retained directions. The indicator does not separate acoustic and hydrodynamic pressure contributions.

Figure 12 compares the radiation indicator, power coefficient, and power-coefficient gradient. For the radiation indicator, θ denotes the corrected source phase θ_s. Phase averaging uses a 360° period for one blade and a 180° period for two blades; the two-blade curves are repeated over 360° in Fig. 12. The gradient $dC_P/d\theta$ is calculated from the phase-averaged power coefficient using periodic central differences on the 2° phase grid. Power-coefficient averaging uses steps 1,200,000–1,500,000 for one blade and 1,200,000–1,550,000 for two, covering approximately 6.6 and 7.7 rotor revolutions, respectively. The two-bladed average thus includes part of the gradual amplitude decay described in Section 4.1. The radiation indicator uses approximately 1.3 and 1.1 revolutions, respectively; these short, unequal records limit the comparison. The cycle-mean radiation indicator for two blades is approximately 2.04 times the one-blade value.

For one blade, the main radiation peak at 40° and the secondary peak at 132° occur near the positive power-coefficient gradient maximum at 52° and the negative minimum at 148°, respectively. The main peak occurs during the upstream blade passage and exceeds the downstream peaks. For two blades, the radiation peaks at 36° and 216° lie near the positive gradient maxima at 58° and 238°, while those at 132° and 312° lie near the negative minima at 146° and 326°. These principal peaks correspond more closely to large gradient magnitudes than to high power coefficients. Exact coincidence is not required: at constant rotational speed, the power-coefficient gradient reflects the rate of change of torque, which is primarily generated by tangential loading. Loading noise depends on the time variation of the aerodynamic force projected toward each observer, including radial loading and rotation of the force direction. The center-based propagation correction also neglects the changing blade-to-observer distance and mean-flow convection.

At the present tip-speed ratio of 4.5, no large-scale dynamic stall is observed in the hybrid simulations. The phase relationships are consistent with radiation associated with rapid changes in aerodynamic loading, as described by the loading-noise formulation (Aihara et al., 2021). The larger two-blade radiation indicator may partly reflect reinforcement of waves from the opposed blades in some observer directions and phases, although this effect is not separated from changes in blade number and loading. The stronger upstream radiation for one blade and the similar principal peak phases suggest that wake interaction may not dominate the principal peaks of this sector-excluded indicator. These interpretations apply to the spanwise-periodic model, which excludes blade-tip vortices and their associated noise.

https://doi.org/10.5194/wes-2026-207
Preprint. Discussion started: 11 November 2026
© Author(s) 2026. CC BY 4.0 License.

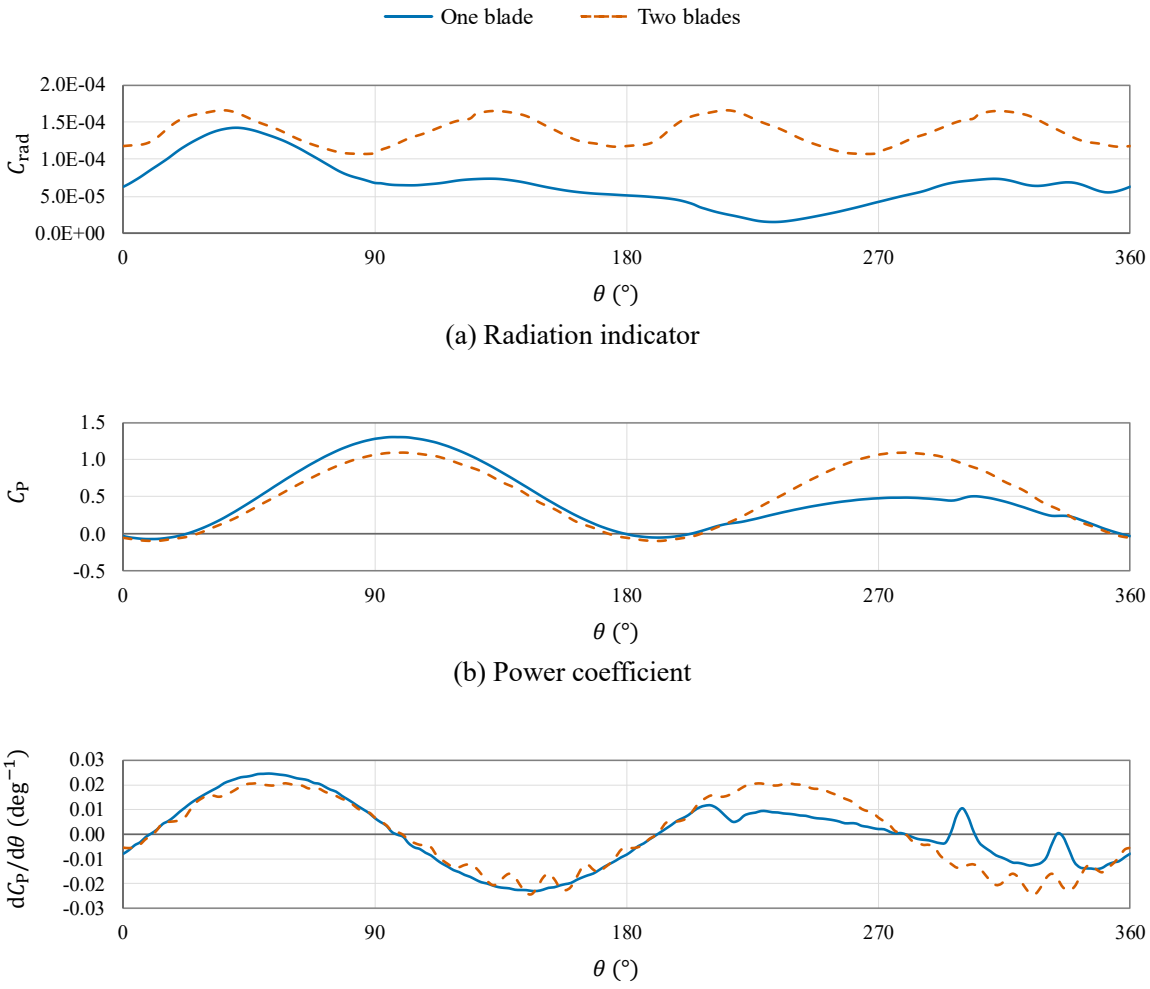


Fig. 12. Phase comparison for one and two blades. (a) Phase-averaged dimensionless radiation indicator C_{rad}; (b) phase-averaged power coefficient C_P; (c) its phase gradient $dC_P/d\theta$. For the radiation indicator in (a), the observer radius is 16 rotor diameters, the ±20° downstream sector is excluded, and the phase is corrected for the propagation delay R/c_s.

5 Conclusions

Three-dimensional direct aeroacoustic simulations were used to examine the relationship between blade number, periodic loading, and pressure radiation from a straight-bladed Darrieus VAWT at a tip-speed ratio of 4.5. The established hybrid LBM–FVLBM method was compared with standard LBM and experimental wake velocities for the two-bladed reference. The one- and two-bladed hybrid calculations then connected changes in power performance with the strength and phase of pressure radiation.

https://doi.org/10.5194/wes-2026-207
Preprint. Discussion started: 11 November 2026
© Author(s) 2026. CC BY 4.0 License.



eawe european academy of wind energy
Open Access WIND ENERGY SCIENCE DISCUSSIONS

Compared with standard LBM, hybrid LBM predicts less extensive low-speed regions near the blades and mean streamwise wake deficits closer to measurements at the representative downstream station. Discrepancies remain in transverse velocity. Both methods predict spectral peaks near the blade-passing frequency and its second harmonic, while standard LBM produces more pronounced peaks over part of the 100–500 Hz range. These differences indicate sensitivity to near-wall resolution and numerical treatment; agreement in wake velocity alone does not validate the acoustic predictions.

The cycle-mean values of the phase-averaged power coefficient are approximately 0.508 for two blades and 0.449 for one blade. At $R/D = 16$, the cycle mean of the phase-averaged radiation indicator, excluding directions within 20° of the downstream direction, is larger by a factor of approximately 2.04. Reinforcement of waves from the opposed blades may contribute to this increase, although its contribution has not been separated from changes in blade number and loading.

For both blade counts, the principal radiation peaks occur near phases of large power-coefficient gradient magnitude rather than at maximum power. The strongest one-blade peak occurs at 40° during the upstream blade passage and exceeds the downstream peaks. At the present tip-speed ratio of 4.5, where no large-scale dynamic stall is observed, these phase relationships are consistent with radiation associated with rapid changes in aerodynamic loading. Exact peak coincidence is not required because torque variations and the observer-directed force variations underlying loading noise are different quantities. The stronger upstream radiation for one blade and similar principal peak phases suggest that wake interaction may not dominate the principal peaks of this sector-excluded indicator.

The radiation indicator compares pressure fluctuations within this setup and does not establish total acoustic power or a noise-optimal blade count. The short, unequal pressure records and the spanwise-periodic geometry limit generalization; blade-tip vortices and shaft and strut effects are excluded. Further work requires longer, matched sampling periods, separate aerodynamic and acoustic convergence studies, experimental pressure validation, and finite-span simulations. Phase-resolved source analysis is needed to quantify the contributions of wave reinforcement and wake interaction.

Code and data availability

The data underlying the phase-resolved comparisons and an independent checking script have been assembled in a local data package, together with file provenance, variable definitions, and reproduction instructions. The package has not yet been deposited in a public repository and has no persistent identifier. The corresponding author can provide these materials on reasonable request. Full three-dimensional flow fields, third-party experimental data, and solver source code are not included in this package. The repository, access conditions, and licenses remain to be finalized before submission.

https://doi.org/10.5194/wes-2026-207
Preprint. Discussion started: 11 November 2026
© Author(s) 2026. CC BY 4.0 License.



eawe european academy of wind energy
Open Access WIND ENERGY SCIENCE DISCUSSIONS

Author contributions

Kazuya Kusano: Conceptualization, Funding acquisition, Methodology, Software, Investigation, Formal analysis, Writing – original draft, Writing – review and editing. Sota Nagatomi: Investigation, Formal analysis, Writing – original draft, Writing – review and editing.

Competing interests

The authors declare that they have no conflict of interest.

Acknowledgements

This work used computational resources of the supercomputer Fugaku provided by RIKEN through the HPCI System Research Project (project IDs hp240258 and hp250305). Parts of the numerical methodology and two-blade results were presented in the ASME Turbo Expo 2026 conference paper by Kusano and Nagatomi (2026). The present study adds a single-blade reference and a phase-resolved comparison of blade-count effects on pressure radiation, power coefficient, and its gradient.
The authors used ChatGPT (OpenAI) to assist with English translation, language editing, manuscript organization, and reference formatting. The authors are responsible for reviewing and verifying the manuscript and take full responsibility for its content.

Financial support

This research was supported by the Ebara Hatakeyama Memorial Foundation. Computational resources were provided through HPCI projects hp240258 and hp250305. The funding and resource providers had no role in study design; analysis or interpretation of the results; manuscript preparation; or the decision to submit the article for publication.

References

Ahnn, S., and Choi, H.: Leading-edge vortex and aerodynamic performance scaling in a simplified vertical-axis wind turbine, Phys. Fluids, 35, 105140, https://doi.org/10.1063/5.0166161, 2023.

Aihara, A., Bolin, K., Goude, A., and Bernhoff, H.: Aeroacoustic noise prediction of a vertical axis wind turbine using large eddy simulation, Int. J. Aeroacoustics, 20, 959-978, https://doi.org/10.1177/1475472X211055179, 2021.

Bangga, G., Dessoky, A., Wu, Z., Rogowski, K., and Hansen, M. O. L.: Accuracy and consistency of CFD and engineering models for simulating vertical axis wind turbine loads, Energy, 206, 118087, https://doi.org/10.1016/j.energy.2020.118087, 2020.

https://doi.org/10.5194/wes-2026-207
Preprint. Discussion started: 11 November 2026
© Author(s) 2026. CC BY 4.0 License.

Botha, J. D. M., Shahroki, A., and Rice, H.: An implementation of an aeroacoustic prediction model for broadband noise from a vertical axis wind turbine using a CFD informed methodology, J. Sound Vib., 410, 389-415, https://doi.org/10.1016/j.jsv.2017.08.038, 2017.

Brandetti, L., Avallone, F., De Tavernier, D., LeBlanc, B., Simão Ferreira, C., and Casalino, D.: Assessment through high-fidelity simulations of a low-fidelity noise prediction tool for a vertical-axis wind turbine, J. Sound Vib., 547, 117486, https://doi.org/10.1016/j.jsv.2022.117486, 2023.

Fei, L., Luo, K. H., and Li, Q.: Three-dimensional cascaded lattice Boltzmann method: Improved implementation and consistent forcing scheme, Phys. Rev. E, 97, 053309, https://doi.org/10.1103/PhysRevE.97.053309, 2018.

Feng, Z. G., and Michaelides, E. E.: The immersed boundary-lattice Boltzmann method for solving fluid–particles interaction problems, J. Comput. Phys., 195, 602-628, https://doi.org/10.1016/j.jcp.2003.10.013, 2004.

Gaitonde, D. V., and Visbal, M. R.: Pade-type higher-order boundary filters for the Navier-Stokes equations, AIAA J., 38, 2103–2112, https://doi.org/10.2514/2.872, 2000.

Geier, M., Greiner, A., and Korvink, J. G.: Cascaded digital lattice Boltzmann automata for high Reynolds number flow, Phys. Rev. E, 73, 066705, https://doi.org/10.1103/PhysRevE.73.066705, 2006.

Ghasemian, M., and Nejat, A.: Aero-acoustics prediction of a vertical axis wind turbine using Large Eddy Simulation and acoustic analogy, Energy, 88, 711-717, https://doi.org/10.1016/j.energy.2015.05.098, 2015.

Graham, W. R., and Pearson, C. E.: Noise from a Model-Scale Vertical-Axis Wind Turbine, AIAA J., 60, 224-235, https://doi.org/10.2514/1.j060531, 2022.

Javaid, M. T., Sajjad, U., Hassan, S. S., Nasir, S., Shahid, M. U., Ali, A., and Salamat, S.: Power enhancement of vertical axis wind turbine using optimum trapped vortex cavity, Energy, 278, 127808, https://doi.org/10.1016/j.energy.2023.127808, 2023.

Kang, S. K., and Hassan, Y. A.: A comparative study of direct-forcing immersed boundary-lattice Boltzmann methods for stationary complex boundaries, Int. J. Numer. Methods Fluids, 66, 1132-1158, https://doi.org/10.1002/fld.2304, 2011.

Kuang, L., Zhang, R., Su, J., Shao, Y., Zhang, K., Chen, Y., Zhang, Z., Tu, Y., Zhou, D., Han, Z., Bao, Y., and Cao, Y.: Systematic investigation of effect of rotor solidity on vertical-axis wind turbines: Power performance and aerodynamics analysis, J. Wind Eng. Ind. Aerodyn., 233, 105284, https://doi.org/10.1016/j.jweia.2022.105284, 2023.

Kusano, K., and Nagatomi, S.: Aeroacoustic investigation of a vertical-axis wind turbine using an overset-grid lattice Boltzmann simulation, in: Proceedings of ASME Turbo Expo 2026: Turbomachinery Technical Conference and Exposition, paper GT2026-175964, Milan, Italy, 15–19 June 2026, 2026.

Kusano, K., Yamada, K., and Furukawa, M.: Aeroacoustic simulation of broadband sound generated from low-Mach-number flows using a lattice Boltzmann method, J. Sound Vib., 467, 115044, https://doi.org/10.1016/j.jsv.2019.115044, 2020.

Kusano, K., Furukawa, M., Sakoda, K., Hatakenaka, K., and Fukui, T.: Hybrid lattice Boltzmann method using Cartesian and body-fitted grids for turbomachinery aeroacoustic simulations, J. Sound Vib., 588, 118516, https://doi.org/10.1016/j.jsv.2024.118516, 2024.

Ottermo, F., Möllerström, E., Nordborg, A., Hylander, J., and Bernhoff, H.: Location of aerodynamic noise sources from a 200 kW vertical-axis wind turbine, J. Sound Vib., 400, 154-166, https://doi.org/10.1016/j.jsv.2017.03.033, 2017.

Pearson, C. E., and Graham, W. R.: Experimental characterization of vertical-axis wind turbine noise, J. Acoust. Soc. Am., 137, EL111-EL116, https://doi.org/10.1121/1.4904915, 2015.

Rezaeiha, A., Kalkman, I., and Blocken, B.: CFD simulation of a vertical axis wind turbine operating at a moderate tip speed ratio: Guidelines for minimum domain size and azimuthal increment, Renew. Energy, 107, 373-385, https://doi.org/10.1016/j.renene.2017.02.006, 2017.

https://doi.org/10.5194/wes-2026-207
Preprint. Discussion started: 11 November 2026
© Author(s) 2026. CC BY 4.0 License.



Rogowski, K., Michna, J., Mikkelsen, R. F., and Ferreira, C. S.: Impact of zigzag tape on blade loads and aerodynamic wake in a vertical axis wind turbine: A Delft VAWT case study, Energy, 321, 135344, https://doi.org/10.1016/j.energy.2025.135344, 2025.

Shubham, S., Wright, N., and Ianakiev, A.: Application of Richardson extrapolation method to aerodynamic and aeroacoustic characteristics of low Reynolds number vertical axis wind turbines, in: 28th AIAA/CEAS Aeroacoustics 2022 Conference, https://doi.org/10.2514/6.2022-3022, 2022.

Shubham, S., Naik, K., Sachar, S., and Ianakiev, A.: Performance analysis of low Reynolds number vertical axis wind turbines using low-fidelity and mid-fidelity methods and wind conditions in the city of Nottingham, Energy, 279, 127904, https://doi.org/10.1016/j.energy.2023.127904, 2023.

Su, J., Lei, H., Zhou, D., Han, Z., Bao, Y., Zhu, H., and Zhou, L.: Aerodynamic noise assessment for a vertical axis wind turbine using Improved Delayed Detached Eddy Simulation, Renew. Energy, 141, 559-569, https://doi.org/10.1016/j.renene.2019.04.038, 2019.

Tescione, G., Ragni, D., He, C., Simão Ferreira, C. J., and Bussel, G. J. W.: Near wake flow analysis of a vertical axis wind turbine by stereoscopic particle image velocimetry, Renew. Energy, 70, 47–61, https://doi.org/10.1016/j.renene.2014.02.042, 2014.

Viqueira-Moreira, M., and Ferrer, E.: Insights into the Aeroacoustic Noise Generation for Vertical Axis Turbines in Close Proximity, Energies, 13, 4148, https://doi.org/10.3390/en13164148, 2020.

Xi, H., Peng, G., and Chou, S. H.: Finite-volume lattice Boltzmann method, Phys. Rev. E, 59, 6202–6205, https://doi.org/10.1103/PhysRevE.59.6202, 1999.

Yushan, R., Zhou, D., Zhang, R., Chen, Y., Kuang, L., Zhang, K., Han, Z., and Zhu, H.: Impact of rotor solidity and blade number on wake characteristics of vertical-axis wind turbines, Phys. Fluids, 37, 015186, https://doi.org/10.1063/5.0249868, 2025.